Structural and Magnetic Transitions in $CaMn_{1-x}W_xO_3$

M. Miclau,[†] J. Hejtmanek,[‡] R. Retoux,[§] K. Knizek,[‡] Z. Jirak,[‡] R. Frésard,[§] A. Maignan,[§] S. Hébert,[§] M. Hervieu,[§] and C. Martin*[,§]

National Institute of Electrochemistry and Condensed Matter, Plautius Andronescu 1, Timisoara, Romania, Institute of Physics of ASCR, Cukrovarnicka 10, 16200 Praha 6, Czech Republic, and Laboratoire CRISMAT, ENSICAEN, CNRS-UMR6508, 6 Boulevard du Maréchal Juin, 14050 Caen Cedex, France

Received April 23, 2007. Revised Manuscript Received June 15, 2007

The perovskite manganites $CaMn_{1-x}W_xO_3$ are studied up to the solubility limit by using transmission electron microscopy, X-ray powder diffraction, and magnetic and transport measurements. The phase diagram shows three compositional regions at low temperatures. As *x* increases, (i) regular *Pnma* perovskite structure and G-type antiferromagnetism (AFM) combined with a weak ferromagnetic (FM) component, (ii) strongly distorted monoclinic $P2_1/m$ structure and C-type AFM associated with orbital ordering, and (iii) strongly distorted *Pnma* structure, associated with charge and orbital ordering and AFM arrangement, are observed. Our measurements demonstrate that each W^{6+} ion creates two extra electron carriers in the Mn^{4+} matrix and appears as a defect in the Mn sublattice. This B-site disorder, together with the lower itinerancy of the doped carriers, make favorable conditions for orbital and/or charge ordering at unusually high critical temperatures (up to 380 K).

Introduction

$CaMnO_3$ crystallizes in a ABO_3 perovskite structure with an orthorhombic distortion due to the tilting of the MnO_6 octahedra (*Pnma* space group with the unit cell $\sqrt{2}a_p \times 2a_p \times \sqrt{2}a_p$, a_p referring to the ideal perovskite). On cooling below room temperature, it undergoes a magnetic transition around 120 K to a G-type antiferromagnetic (AFM) state, where each Mn spin is surrounded by six AFM coupled neighbors.[1−5] By a heterovalent substitution on the Ca or Mn sites, a small amount of Mn^{3+} in the Mn^{4+}matrix is created, which drastically changes the behavior of the compounds. In most studies, it is achieved by Ln^{3+} for Ca^{2+} substitution, according to $Ca^{2+}_{1-x}Ln^{3+}_xMn^{4+}_{1-x}Mn^{3+}_xO_3$.[6−17] But it can also be done by substituting Mn by cations of valence higher than +4, such as $CaMn^{4+}_{1-2x}Mn^{3+}_xM^{5+}_xO_3$ (with M = Nb, Ta, or V)[18−20] or $CaMn^{4+}_{1-3x}Mn^{3+}_{2x}M^{6+}_xO_3$ (for M = Mo or W).[21−24]

Studies of some $Ca^{2+}_{1-x}Ln^{3+}_xMn^{4+}_{1-x}Mn^{3+}_xO_3$ compounds have shown a systematic evolution of the behaviors versus *x*. For low Mn^{3+} levels, up to about 10%, the paramagnetic (PM) state of the room-temperature (RT) phase is transformed at about 110 K into a complex magnetic state, which may be attributed either to a spin canting in the G-type AFM phase or to a segregation of ferromagnetic (FM) regions in the AFM matrix. Several studies have shown that the second description is the more probable.[8,11,12,13] This kind of phase separation is also in accordance with the original idea of Goodenough that the doped e_g electrons are confined to a restricted space because of the electric field effect of randomly distributed A cations.[2] For higher Mn^{3+} contents, an orthorhombic to monoclinic transition is observed at low

* Corresponding author. E-mail: christine.martin@ensicaen.fr. Fax: 33 (0)2 31 95 16 00.
[†] National Institute of Electrochemistry and Condensed Matter.
[‡] Institute of Physics of ASCR.
[§] Laboratoire CRISMAT, ENSICAEN.

(1) Wollan, E. O.; Koehler, W. C. *Phys. Rev.* **1955**, *100*, 545.
(2) Goodenough, J. B. *Phys. Rev.* **1955**, *100*, 564.
(3) Mac Chesney, J. B.; Williams, H. J.; Potter, J. F.; Sherwood, R. C. *Phys. Rev.* **1967**, *164*, 779.
(4) Poeppelmeier, K. R.; Leonowicz, M. E.; Scanlon, J. C.; Longo, J. M.; Yelon, W. B. *J. Solid State Chem.* **1982**, *45*, 71.
(5) Jirak, Z.; Krupicka, S.; Simsa, Z.; Dlouha, M.; Vratislav, S. *J. Magn. Magn. Mater.* **1985**, *53*, 153.
(6) Maignan, A.; Martin, C.; Damay, F.; Raveau, B. *Chem. Mater.* **1998**, *10*, 950.
(7) Maignan, A.; Martin, C.; Damay, F.; Raveau, B.; Hejtmanek, *J. Phys. Rev. B* **1998**, *58*, 2758.
(8) Martin, C.; Maignan, A.; Hervieu, M.; Raveau, B.; Jirak, Z.; Kurbakov, A.; André, C.; Bourée, F. *J. Magn. Magn. Mater.* **1999**, *205*, 184.
(9) Hagdorn, K.; Hohlwein, D.; Ihringer, J.; Knorr, K.; Prandl, W.; Ritter, H.; Schmid, H.; Zeiske, Th. *Eur. Phys. J. B* **1999**, *11*, 243.
(10) Martin, C.; Maignan, A.; Hervieu, M.; Raveau, B.; Jirak, Z.; Savosta, M. M.; Kurbakov, A.; Trounov, V.; André, G.; Bourée, F. *Phys. Rev. B* **2000**, *62*, 6442.
(11) Savosta, M. M.; Novak, P.; Marysko, M.; Jirak, Z.; Hejtmanek, J.; Englich, J.; Kohout, J.; Martin, C.; Raveau, B. *Phys. Rev.* **2000**, *62*, 9532.
(12) Ling, C. D.; Granado, E.; Neumeier, J. J.; Lynn, J. W.; Argyriou, D. N. *Phys. Rev. B* **2003**, *68*, 134439.
(13) Granado, E.; Ling, C. D.; Neumeier, J. J.; Lynn, J. W.; Argyriou, D. N. *Phys. Rev. B* **2003**, *68*, 134440.
(14) Pissas, M.; Kallias, G.; Hofmann, M.; Többens, D. M. *Phys. Rev. B* **2003**, *65*, 064413.
(15) Pissas, M.; Kallias, G. *Phys. Rev. B* **2003**, *68*, 134414.
(16) Troyanchuck, I. O.; Samsonenko, N. V.; Szymczak, H.; Nabaliek, A. *J. Solid State Chem.* **1997**, *131*, 144.
(17) Hervieu, M.; Barnabé, A.; Martin, C.; Maignan, A.; Damay, F.; Raveau, B. *Eur. Phys. J.* **1999**, *B8*, 31.
(18) Raveau, B.; Zhao, Y.; Martin, C.; Hervieu, M.; Maignan, A. J. *Solid State Chem.* **2000**, *149*, 203.
(19) . Guo, Y.; Li, W.; Roy, S.; Ali, N. *Chem. Mater.* **2005**, *17*, 2735.
(20) Ang, R.; Sun, Y. P.; Ma, Y. Q.; Zhao, B. C.; Zhu, X. B.; Song, W. H. *J. Appl. Phys.* **2006**, *100*, 063902.
(21) Martin, C.; Maignan, A.; Hervieu, M.; Raveau, B.; Hejtmanek, J. *Phys. Rev. B* **2001**, *63*, 100406 (R).
(22) Maignan, A.; Martin, C.; Autret, C.; Hervieu, M.; Raveau, B.; Hejtmanek, J. *J. Mater. Chem.* **2002**, *12*, 1806.
(23) Maignan, A.; Martin, C.; Autret, C.; Hervieu, M.; Raveau, B. *J. Appl. Phys.* **2002**, *91*, 4267.
(24) Pi, L.; Hébert, S.; Martin, C.; Maignan, A.; Raveau, B. *Phys. Rev. B* **2003**, *67*, 024430.

10.1021/cm0710958 CCC: $37.00
Published on Web 07/28/2007

temperature, which corresponds to the setting of the C-type AFM,[1,2,4,10,12,13] which can be described as an AFM coupling of FM chains. The MnO_6 octahedra are elongated along these chains, expressing the orbital ordering (OO). A further increase in the e_g electron density tends to occur in charge- and orbital-ordered (CO/OO) Mn^{3+}/Mn^{4+} structures, associated with a more complex parquetlike AFM order.[17,25,26]

Similar trends are observed for the Mn-site-substituted series (successively G-type AFM with a small FM component, C-type AFM, and charge-ordered AFM states appear with the increase in Mn^{3+} content), but there are some important distinctions. In the previous case of the A-site substitution, the doped electrons tend to migrate over equivalent Mn sites in the vicinity of the A-site substituant. On the other hand, the A-sublattice remains intact in the Mn-site-substituted manganites, and the heterovalent substituants in Mn-sites represent static pointlike defects, i.e., scattering centers for the charge delocalization. It may be favorable for electron localization phenomena, and indeed, previous reports on the $CaMn_{1-x}Mo_xO_3$ system demonstrated the onset of CO/OO phases at unusually high temperatures, around RT.[21,23] To go further in details in the understanding of parameters governing the behavior in Mn-site-substituted systems, we have undertaken a comprehensive investigation of the analogous $CaMn_{1-x}W_xO_3$ series. By combining structural characterizations (X-ray diffraction and electron microscopy versus temperature) and magnetic and transport measurements (magnetization, susceptiblity, resistivity, thermoelectric power), we present a new magnetic and structural phase diagram, showing that the charge and/or orbital ordering develops at unusually high temperatures ($\gg$RT).

Experimental Section

The synthesis of the $CaMn_{1-x}W_xO_3$ samples with $0 < x \leq 0.20$ has been previously described.[18] The samples were prepared by solid-state reaction at 1500 °C in air, starting from stoichiometric mixtures of CaO, MnO_2, and WO_3.

All the samples were characterized by X-ray powder diffraction at room temperature. The patterns were obtained using a Xpert Philips diffractometer (Cu Kα). The temperature-dependent structural characterization over the range 300−450 K was also realized for the $x = 0.10$ and 0.15 compositions using a X-ray diffractometer Bruker D8 (Cu Kα, energy-dispersive SOL-X detector) equipped with a MRI TC wide range temperature chamber. Two scans were measured for each temperature and the measured intensities were compared in order to check the thermal stability and reproducibility of the sample structure. All X-ray diffraction patterns were analyzed using the Rietveld profile analyzing method with help of FULLPROF program package.[27]

Specimens for transmission electron microscopy (TEM) observations were prepared crushing the crystallites in ethanol. A drop of the suspension is deposited and dried onto a carbon-coated copper grid. The TEM study was performed in 200 kV JEOL 2010 FEG and JEOL 2010 transmission electron microscopes fitted with double-tilt liquid-nitrogen-cooled sample holders (tilt ± 30°). The cationic composition of the materials was confirmed by energy-dispersive X-ray analysis (EDX) using EDAX and OXFORD EDX spectrometers coupled with the microscopes.

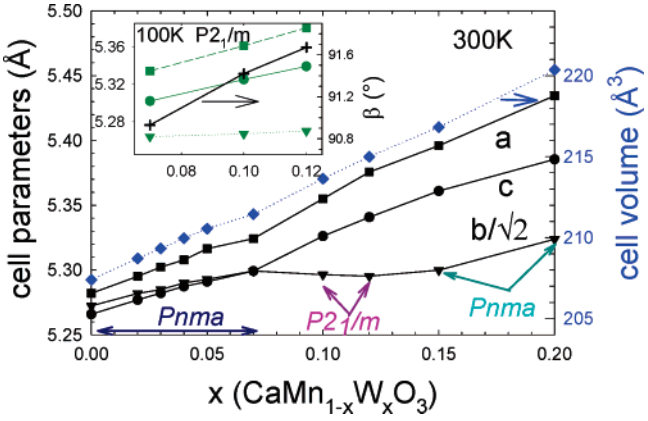

Figure 1. Evolution of the room-temperature lattice parameters (left *y*-axis) and cell volume (right *y*-axis and dotted line) vs the W-content (x), determined from X-ray powder diffraction. The space groups used for refining the data are given in the picture. In the inset, some structural parameters (a, b, c, and β) obtained by refining (in the $P2_1/m$ space group) X-ray data acquired at 100 K are plotted for 3 compositions.

The magnetic susceptibility measurements in the temperature range 5−400 K were generally performed in applied field of 1.45 T on zero-field-cooled (ZFC) and field-cooled (FC) samples. In selected cases, magnetization curves up to 5 T were taken at low temperatures. All these DC magnetic experiments were performed using a SQUID magnetometer. In addition, high-temperature susceptibility was measured up to 800 K using a pendulum magnetometer in an applied field of 1.8 T.

The thermoelectric power (TEP) and electrical resistivity measurements were carried out using a homemade system within the temperature range 15−850 K. The four-point steady-state method with separated sensors and power contacts was applied, the details of both low-temperature (15−320 K) and high-temperature (300−850 K) measurements were reported previously.[28]

Results

Structural Study. *X-ray Characterization.* The room-temperature X-ray patterns show that the samples are single phased with a distorted perovskite structure for $x < 0.20$. For higher W contents ($x \geq 0.2$), scheelite $CaWO_4$[29] and/or double perovskite Ca_2MnWO_6[30] appear as impurities, independently of the synthesis process.

The evolution of the room-temperature lattice parameters versus x is reported in Figure 1. The unit-cell volume increases with increasing tungsten content, but it is attributed to the formation of larger Mn^{3+} ions in the Mn^{4+} sites rather than to the ionic size of W^{6+}.[31] For x varying from 0 to 0.07, the X-ray patterns are refined in the *Pnma* space group with unit-cell parameters $a \approx a_p\sqrt{2}$, $b \approx 2a_p$, and $c \approx a_p\sqrt{2}$. The orthorhombic distortion characteristic for this O type perovskite structure ($a > b/\sqrt{2} \approx c$) reflects the octahedral tilt that increases with x. The *Pnma* symmetry is preserved down to the lowest temperature except for the $x = 0.07$ sample, which undergoes a transition to a monoclinic phase at around

(25) Fernandez-Diaz, M. T.; Martinez, J. L.; Alonso, J. M.; Herrero, E. *Phys. Rev. B* **1999**, *59*, 1277.
(26) Jirak, Z.; Martin, C.; Hervieu, M.; Hejtmanek, *J. Appl. Phys. A* **2002**, *74*, S1755.
(27) http://journals.iucr.org/iucr-top/comm/cpd/Newsletters/ or http://www.ill.fr/pages/science/IGroups/diff/Soft/fp/.
(28) Autret, C.; Hejtmanek, J.; Knizek, K.; Marysko, M.; Jirak, Z.; Dlouha, M.; Vratislav, S. *J. Phys.: Condens. Matter* **2005**, *17*, 1601.
(29) Zalkin, A.; Templeton, D. H. *J. Chem. Phys.* **1964**, *40*, 501.
(30) Azad, A. K.; Ivanov, S. A.; Eriksson, S. G.; Eriksen, J.; Rundlöf, H.; Mathieu, R.; Svedlindh, P. *Mater. Res. Bull.* **2001**, *36*, 2485.
(31) Shannon, R. D. *Acta Crystallogr., Sect. A* **1976**, *32*, 751.

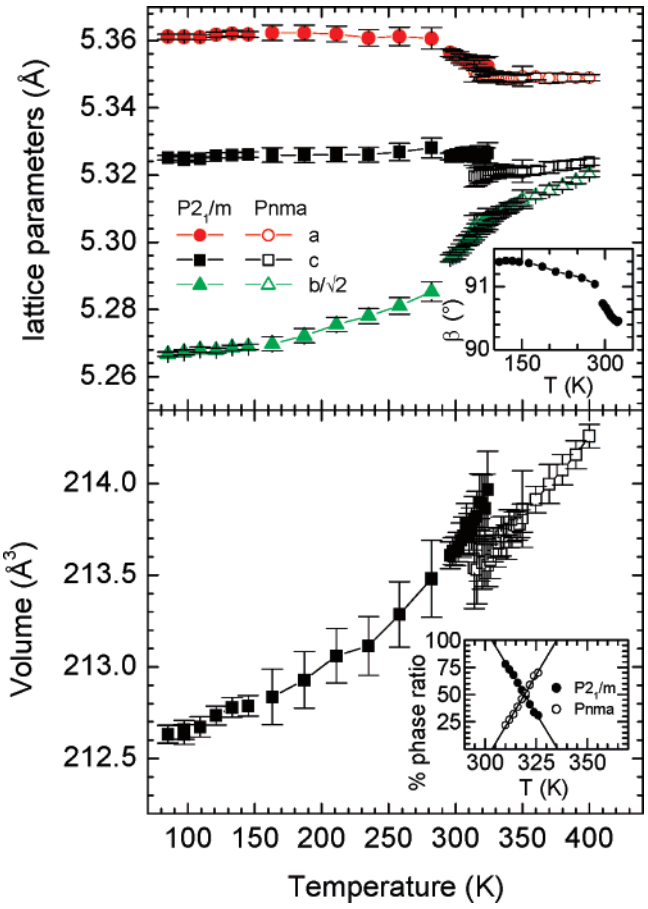

Figure 2. Upper panel: Temperature dependence of the unit-cell parameters (*a*, *b*, and *c*) vs temperature for $x = 0.10$; the evolution of β is given in the inset. Lower panel: Corresponding cell-volume evolution and phase ratio in inset.

180 K. The compounds $x = 0.10$ and 0.12 exhibit the same kind of monoclinic distortion existing already at RT. The patterns are refined in the $P2_1/m$ space group with cell parameters *a*, *b*, *c* of values similar to those of the orthorhombic *Pnma* region, but with a monoclinic angle β significantly deviating from 90°. This deformation makes one of the [101] diagonals elongated, whereas the second one is shortened, leading the ferrodistortive arrangement of elongated MnO_6 octahedra, typical for OO in the C-type AFM manganites.[8] The compounds with $x = 0.15$ and 0.20 (even if small peaks of impurity appear for the latter composition) are also characterized by the *Pnma* cell (as for the small *x* values) but with a pronounced contraction of the *b* parameter relative to the *a* and *c* parameters. This kind of lattice deformation reflects the antiferrodistortive arrangement of elongated $Mn^{3+}O_6$ octahedra in the *ac* plane, which is typical for CO/OO manganites.[32]

The X-ray diffraction measurements thus allow us to distinguish three structural regions versus x − regular *Pnma*, strongly distorted $P2_1/m$, and strongly distorted CO phase with *Pnma* subcell. Nevertheless, the boundaries between the three zones vary with temperature.

In Figure 2, the evolution of the lattice parameters versus temperature is reported for $x = 0.10$. A biphasic region is visible between ∼300 and 330 K, corresponding to the *Pnma* to $P2_1/m$ transition. The evolution of the lattice parameters vs *T* reported in Figure 3 for $x = 0.15$ is rather continuous through the CO/OO transition.

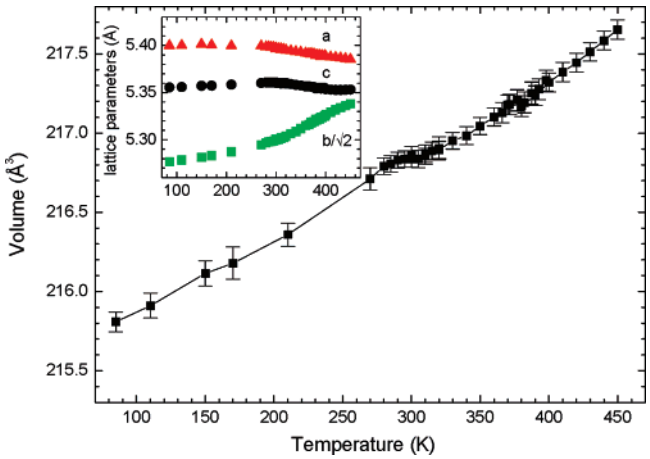

Figure 3. Temperature dependence of the cell volume (*Pnma*) for $x = 0.15$; in inset, corresponding cell parameters vs *T*.

The succession of the orthorhombic, monoclinic, and CO phases (versus *x*) is analogous to that reported for other Mn^{4+}-rich manganites obtained by A- or B-site substitution. The orthorhombic to monoclinic distortion is associated with orbital polarization of e_g electron density that becomes cooperative because of long-range elastic interactions. Consequently, the orbital ordering is not sensitive to the disorder induced by W-for-Mn substitution. Moreover, the transition temperatures are higher than those in the A-site-substituted compounds. On the other hand, the charge ordering with essentially antiferrodistortive arrangement of local MnO_6 distortions is driven by interactions between nearest and next-nearest neighbors, and its occurrence in samples with high concentration of W and thus of defects in the Mn sublattice remains puzzling. To investigate these W-based manganites in more detail, we have performed an electron microscopy study.

Electron Microscopy Study. The existence of three structural regions is also shown by electron diffraction (ED). For the smaller *x* values ($0 \leq x \leq 0.05$), the ED confirms the *Pnma* space group at RT and that no structural transition is observed at low temperature (92 K, as shown Figure 4).

In the intermediate part of the phase diagram for $0.07 \leq x \leq 0.12$, a *Pnma* symmetry is observed at high temperature, whereas a structural transition (to $P2_1/m$) is systematically observed with decreasing temperature. The [010] ED pattern recorded at room temperature for the $x = 0.1$ compound (Figure 5a) shows the typical splitting of the spots due to the twinning phenomena occurring as soon as the monoclinic $P2_1/m$ symmetry appears. The associated dark-field image (Figure 5b) shows the twinning domains below T_{OO}, the image of the same area recorded at 400 K (i.e., above T_{OO}) is given in insert.

In the third part (for larger *x*), the ED patterns recorded below T_{CO} present extra satellites appearing around the main Bragg spots attributed to the *Pnma* space group. The satellites point to a structural modulation that is associated with CO/OO. Figure 6a illustrates this feature, with the [010] ED pattern recorded at room temperature for the $x = 0.14$

(32) Radaelli, P. G.; Cox, D. E.; Marezio, M.; Cheong, S. W. *Phys. Rev. B* **1997**, *55*, 3015.

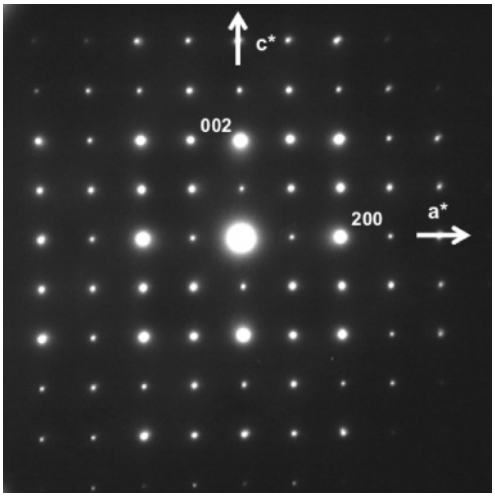

Figure 4. [010] Typical *Pnma* electron diffraction pattern recorded for the smaller x values of the $CaMn_{1-x}W_xO_3$ series (in this case $x = 0.04$ and 92K). *h00*, $h = 2n + 1$ and 00l, $l = 2n + 1$ are highlighted by double diffraction phenomena.

compound. The modulation vector is parallel to the $\vec{a}^*$ axis and possesses an incommensurate value of the modulation, $\vec{q} \cong 0.23\vec{a}^*$. On this ED pattern, the weak satellites apparently observed along the $\vec{c}^*$ direction are in fact due to the presence of twinned domains disoriented to one another by 90° in the crystals. In images b and c in Figure 6, the [010] images recorded at room temperature present a modulation of the contrast with a periodicity in good agreement with the $\vec{q}$ vector deduced from the ED observations. In that part of the phase diagram, the experiments show that the CO develops at relatively high T_{CO} (>RT), for example, the evolution of the modulation value versus temperature is presented in Figure 6d. At low-temperature, it remains stable and close to 0.23. The observation of a *Pnma* subcell with extra spots at $\cong 0.23a^*$ by electron diffraction is in agreement with the refining of the RT X-ray pattern in a *Pnma* subcell. For the $x = 0.14$, 0.15, and 0.16 samples, the electron diffraction observations lead to a similar ~0.23 value at 92 K.

All these structural phenomena are quite similar to those observed for the Mo substituted calcium manganese series in the same range of x values.[21]

Magnetic Properties. The G-type AFM ground state of $CaMnO_3$ is associated with a weak ferromagnetism due to the Dzyaloshinskii−Moriya interactions or oxygen nonstoichiometry.[1–5] As shown in Figure 7, the observed magnetization in an applied magnetic field of 1.45 T at 4 K is about 0.04 μ_B per Mn. As x is slowly increased in $CaMn_{1-x}W_xO_3$, the magnetization value increases, reaches a maximum around 0.4 μ_B for $x = 0.04$, and then drops to a value smaller than that of $CaMnO_3$ (Figure 7). Ferromagnetism in these compounds is explained by the fact that the substitution with W introduces mobile electrons into the e_g band, so that the interactions of these carriers via t_{2g} spins induce ferromagnetic coupling. Even if the magnetization is recalculated per Mn atom and not for the formula unit (Mn + W) as shown in Figure 7, the maximal observed moment is smaller than the one of about 1.0 μ_B reported for the electron-doped manganites $Ca_{1-x}Ln_xMnO_3$ for a similar Mn^{3+}/Mn^{4+} ratio (around 0.08−0.10).[6] For these compounds, the low-temperature magnetic state was described as FM clusters in a G-type AFM matrix. The small value of the magnetization indicates that the FM interactions are weaker in these Mn-substituted manganites, in connection with the d^0 configuration of W^{6+}, which limits the double exchange (DE) in the Mn sublattice.

For $x \geq 0.07$, no spontaneous FM moment is detected in the magnetization measurements. The magnetic susceptibility curves in Figure 8 show two distinct anomalies, also observable by the thermoelectric power measurements presented below. For $x = 0.10$ and 0.12, the anomaly at high temperature corresponds to the monoclinic transition, whereas the anomaly at lower temperature (around 170 K) is related to the ordering of the C-type AFM (see the neutron diffraction study on analogous compound $CaMn_{0.9}Mo_{0.1}O_3$[22]). These compounds thus remain in the paramagnetic state on cooling below the orbital-ordering temperature until T_N, which does not vary (around 170 K), whereas T_{OO} varies from 320 K for $x = 0.10$ to 370 K for $x = 0.12$. It is remarkable that this OO state develops at unusually high temperature, significantly larger than the maximum observed in the $Ca_{1-x}Pr_xMnO_3$ and $Ca_{1-x}Sm_xMnO_3$ systems, where orbital ordering is coupled with the onset of C-type AFM order, $T_{OO} \approx T_N \approx 140$ K. For the $x = 0.07$ sample, it is not so clear on the susceptibility curve, but two anomalies can be also detected, meaning that structural and magnetic orders remain decoupled.

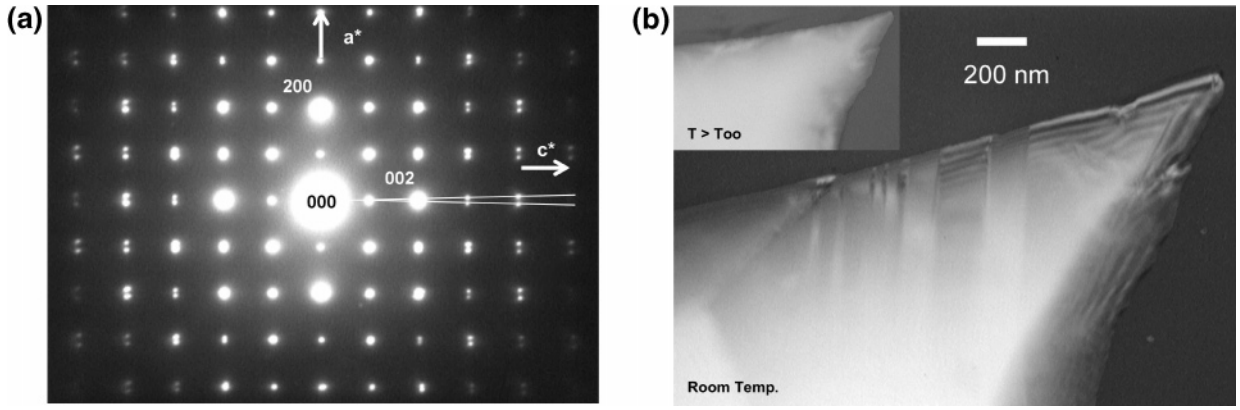

Figure 5. $CaMn_{0.90}W_{0.10}O_3$ (a) [010] electron diffraction pattern recorded at RT. The white lines drawn on the ED pattern show the splitting of the spots correlated to the establishment of the monoclinic $P2_1/m$ structure below T_{OO}. (b) [010] image recorded at RT. The parallel domains associated with the appearance of the monoclinic distortion are clearly observed. In insert, on the same part of the crystal, the parallel domains have totally disappeared at 400 K (i.e., above T_{OO}), and the structure presents a *Pnma* symmetry.

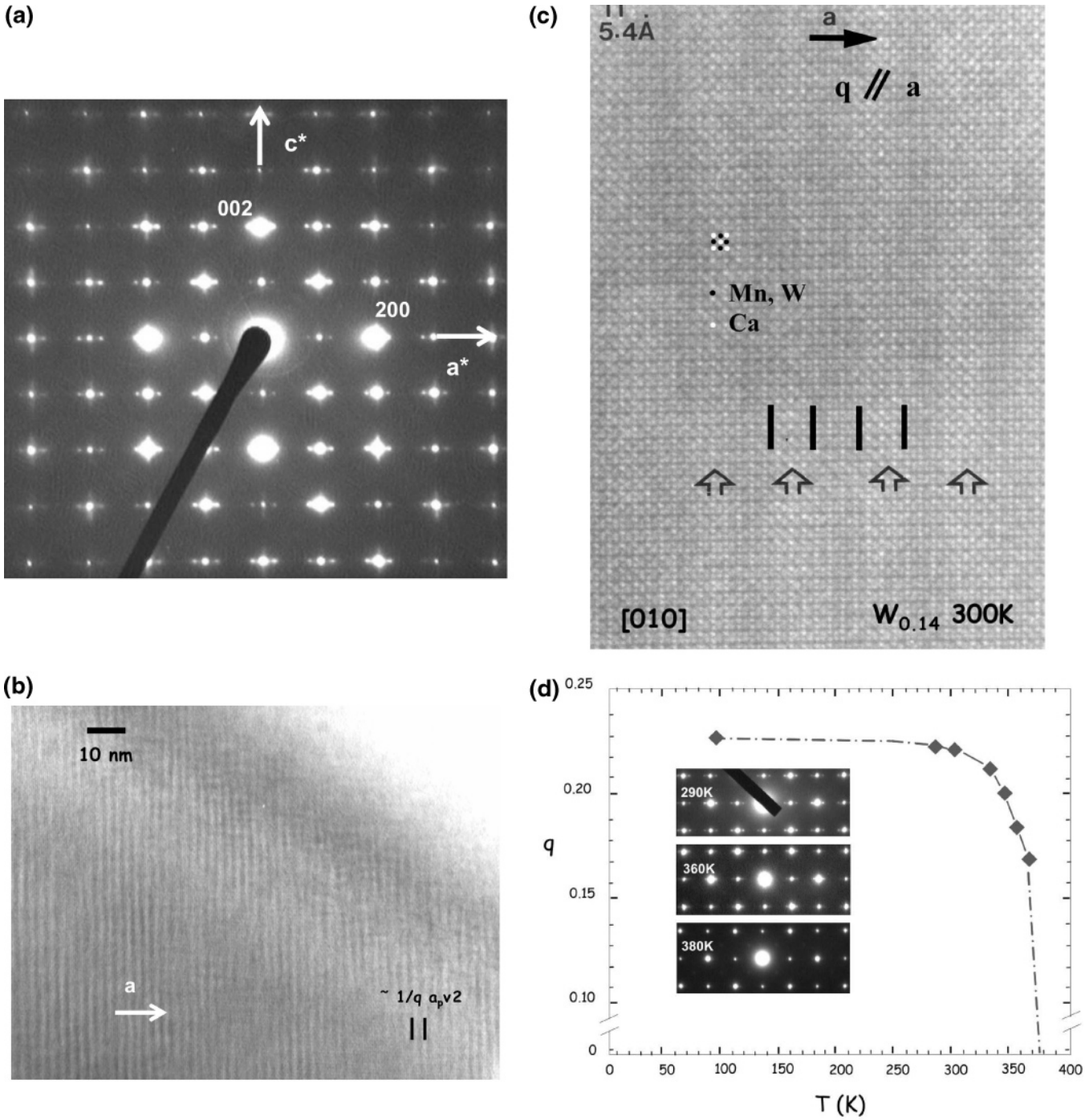

Figure 6. $CaMn_{0.86}W_{0.14}O_3$ (a) ED pattern recorded at room temperature characteristic of the charge-ordered state observed in the third part of the phase diagram. The satellites characteristic of the incommensurate structure are systematically observed around the main spots of the ED pattern. The q value is close to 0.23. The weak satellites appearing along c^* are due to ED pattern superposition of 90° oriented domains. (b) Lattice image associated with Figure 6a showing stripes attesting that the modulation is well-established in quite large zones of the crystal at room temperature. The periodicity of the contrast is in good agreement with the q value deduced from ED. (c) Enlargement of (b); on this HREM, image one can note that the structure of the stripes is not so regular. The incommensurate aspect of the modulation has to be connected with the local variations of the contrast. (d) Evolution of the amplitude of the modulation vector vs T (temperature increasing from 92 to 400 K); inset ED patterns recorded above room temperature are presented to show the disappearance of the satellites at T_{CO}.

For the $x = 0.15$ sample, presented in Figure 8, the anomalies at high- and low-temperature reflect the charge/orbital ordering and the onset of magnetic order, respectively, $T_{CO} \approx 380$ K and $T_N \approx 120$ K.

Transport Properties. The temperature dependence of the electrical resistivity and thermopower of the $CaMn_{1-x}W_xO_3$ series is shown in Figures 9−11. In Figure 9, the measurements for $x = 0.02$, 0.04, and 0.07 are compared with our earlier data on A-site-substituted manganites ($CaMnO_3$, $Ca_{0.975}Pr_{0.025}MnO_3$, $Ca_{0.95}Sm_{0.05}MnO_3$, and $Ca_{0.90}Sm_{0.10}MnO_3$[33,34]). It is seen that the electron doping, which induces a decrease in the RT resistivity, quickly changes the semiconducting character of $CaMnO_3$. In the case of $Ca_{0.975}Pr_{0.025}MnO_3$, for instance, the resistivity value decreases slightly with decreasing temperature down to about 150 K in a metalliclike manner and finally turns up because of localization in AFM region at lower temperatures. In the same way, the RT value of the thermopower drops from

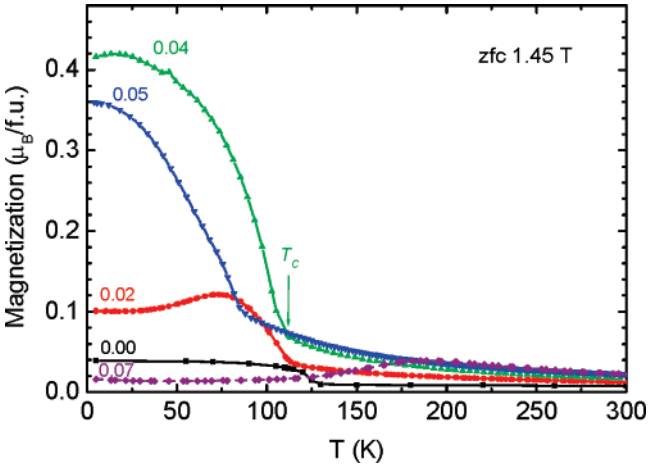

Figure 7. Magnetic moment vs temperature, measured on zero-field-cooled samples with $x = 0$, 0.02, 0.04, 0.05, and 0.07 on heating in 1.45 T, T_C is shown by a vertical arrow for $x = 0.04$.

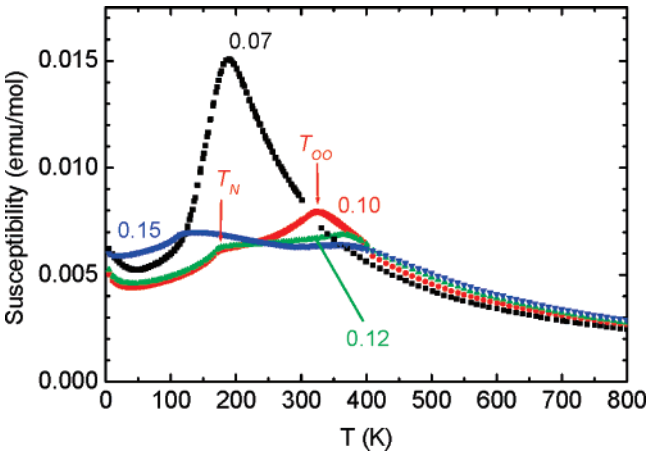

Figure 8. $CaMn_{1-x}W_xO_3$: Magnetic susceptibility vs temperature, deduced from magnetization measured in 1.45 T and zfc mode. The x values are given in the graph; T_N and T_{OO} are indicated with vertical arrows for the $x = 0.10$ sample.

about −800 μV/K (for $CaMnO_3$) to −200 μV/K (for $Ca_{0.975}Pr_{0.025}MnO_3$). For the latter, the thermoelectric power exhibits a linear (metallic) dependence versus temperature and a marked localization is observed at $T_N = 115$ K, which reflects the AFM matrix properties. Similar trends are observed for $Ca_{0.95}Sm_{0.05}MnO_3$, whereas $Ca_{0.90}Sm_{0.10}MnO_3$ shows a clear decrease in both the electrical resistivity and thermopower below 115 K, pointing to an electric percolation of the more conducting FM regions formed in the AFM matrix. Concerning the $CaMn_{1-x}W_xO_3$ system, there is also a systematic decrease of resistivity and thermopower at RT from $x = 0.02$ to $x = 0.07$. However, the resistivity values are about 1 order of magnitude higher and the metalliclike decrease in resistivity is not achieved for samples $x = 0.02$ and 0.04 despite the relatively large e_g electron doping of 4 and 8%, respectively. Both $x = 0.02$ and 0.04 samples show a localization below 115 K associated with AFM ordering and segregation of the non-percolating FM regions detected by magnetic measurements, as mentioned above. The sample x = 0.07 exhibits a more marked localization at 180 K, both in resistivity and thermopower, that is attributed to the onset of the ferrodistortive orbital ordering, prerequisite for the C-type magnetic order.

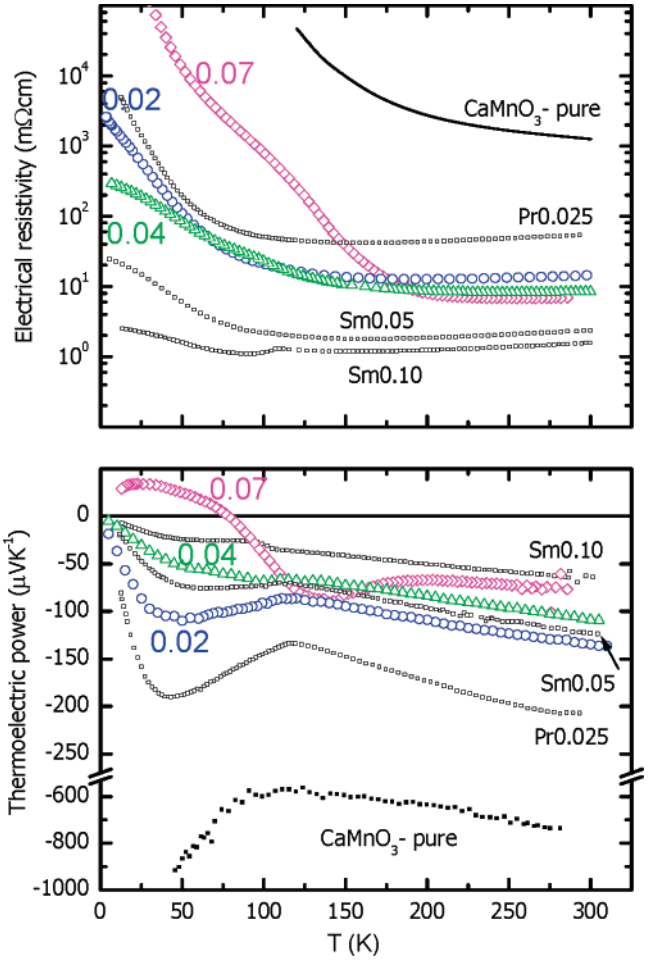

Figure 9. Temperature dependence of electrical resistivity (up) and thermopower (down) for $CaMn_{1-x}W_xO_3$ with $x = 0.02$, 0.04, and 0.07 compared with $CaMnO_3$, $Ca_{0.975}Pr_{0.025}MnO_3$, $Ca_{0.95}Sm_{0.05}MnO_3$, and $Ca_{0.90}Sm_{0.10}MnO_3$.

The transport data of samples $x = 0.07$, 0.10, and 0.12 are summarized in Figure 10, where $Ca_{0.80}Sm_{0.20}MnO_3$ data are added for comparison.[34] Above T_{OO}, the linear metalliclike temperature dependence of both resistivity and thermopower is observed. A negative sign and decreasing slope (dS/dT) of thermopower with x point to an increasing concentration of electronlike charge carriers. Onset of orbital order is accompanied with localization in resistivity and thermopower. For the samples $x = 0.07$ and 0.10, there is a marked upturn of the thermopower at low temperatures, followed by a sign change from negative toward positive values. The positive value of the thermopower at the lowest temperatures points to a holelike character of charge carriers in the conducting FM chains of the C-type AFM phase.[22]

The measurements of the sample $x = 0.15$ are presented in Figure 11. The increased resistivity and the change from a metallic to a semiconducting character at high temperatures reflect the Mn-sublattice defects induced by the high content of W. The thermopower is temperature independent and close to −50 μV/K. Localization due to charge ordering occurs at $T_{CO} \approx 380$ K, which corresponds well with the susceptibility

(33) Savosta, M. M.; Novák, P.; Maryško, M.; Jirák, Z.; Hejtmánek, J.; Englich, J.; Kohout, J.; Martin, C.; Raveau, B. *Phys. Rev. B* **2000**, *62*, 9532.
(34) Hejtmanek, J.; Jirák, Z.; Maryško, M.; Martin, C.; Maignan, A.; Hervieu, M.; Raveau, B. *Phys. Rev. B* **1999**, *60*, 14057.

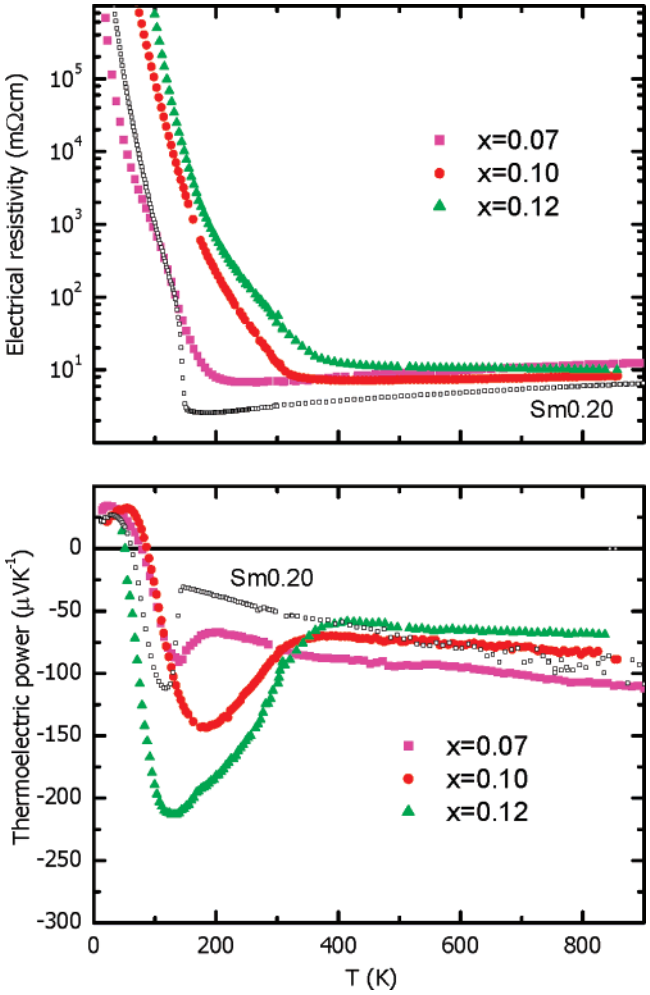

Figure 10. Temperature dependence of electrical resistivity (up) and thermopower (down) for $CaMn_{1-x}W_xO_3$ with $x = 0.07$, 0.10, and 0.12, compared with $Sm_{0.2}Ca_{0.8}MnO_3$ (as a reference for the C-type AFM behavior).

change in Figure 8. Down to the lowest measurable temperatures, the thermopower remains negative and its absolute value increases markedly below T_N. This behavior points to an enhanced localization of the electronlike charge carriers and is clearly distinguishable from the holelike conduction characterizing the FM chains of the C-type phase.

Discussion and $CaMn_{1-x}W_xO_3$ Phase Diagram. The (T,x) structural and magnetic phase diagram of the $CaMn_{1-x}W_xO_3$ system is drawn in Figure 12 (for $0 \leq x \leq 0.16$) by using the results of transmission electron microscopy, X-ray powder diffraction, and magnetic and transport measurements. Because of the lack of neutron diffraction data, the low-temperature magnetic structures are determined by comparison of the structural and physical properties of this W-system with the results obtained for the analogous Mo series, for which neutron diffraction data are available. Gradually increasing x, three compositional regions can be distinguished. For small x, the structure remains *Pnma*, and at low temperatures, a transition from a PM to a AFM state with a small FM component is observed at about 110 K, whatever x. The intermediate region extends roughly from $x \cong 0.07$ to $x \cong 0.12$. With decreasing temperature, a structural transition from *Pnma* to $P2_1/m$ is first observed, corresponding to the setting of the orbital ordering. Below this temperature, a magnetic transition from PM to AFM

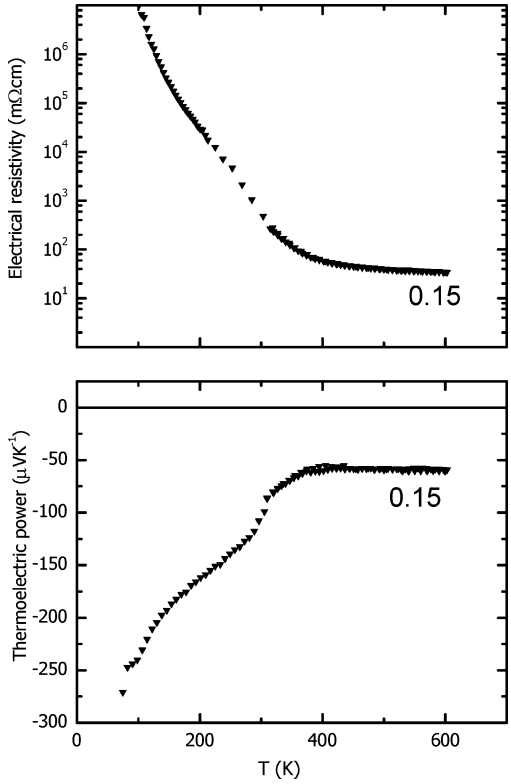

Figure 11. Temperature dependence of electrical resistivity (up) and thermopower (down) for $CaMn_{0.85}W_{0.15}O_3$.

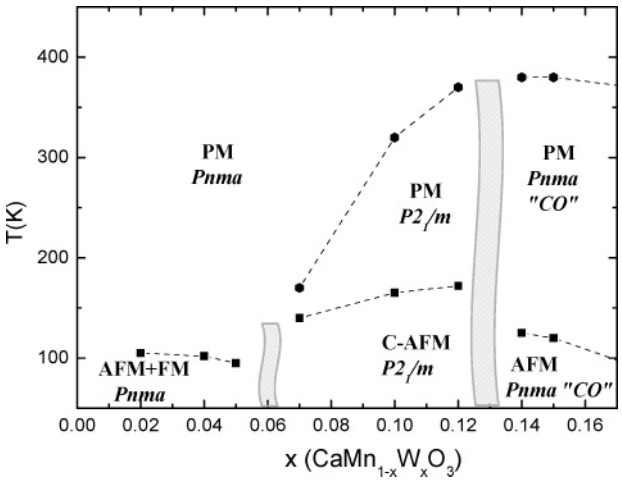

Figure 12. (T,x) structural and magnetic phase diagram of the $CaMn_{1-x}W_xO_3$ series. The space groups are given (*Pnma* and $P2_1/m$), and CO stands for charge ordering; PM, AFM, and FM are for para-, antiferro-, and ferromagnetism, respectively.

(C-type) appears. The structural transition temperature increases strongly with x and exceeds room temperature for higher x values, whereas T_N increases only slightly, keeping the magnetic ordering temperature close to 150 K. The third region ($x \geq 0.13$) is the domain of charge- and orbital-ordered phases. The charge ordering originates well above RT and is associated with a structural modulation characterized by the wave vector $\vec{q} \cong 0.23\vec{a}^*$. The AFM order sets in at much lower temperature. It bears strong similarity to that reported for the A-site-substituted systems $Ca_{0.75}Pr_{0.25}MnO_3$[26] or $Ca_{0.75}La_{0.25}MnO_3$[35] with 1:3 Mn^{3+}:Mn^{4+} order and a modulation vector $\vec{q} = 0.25\vec{a}^*$. Both transition temperatures T_{CO} and T_N decrease slightly when x increases.

The observed phase diagram shows a strong analogy to that previously reported for related system with another hexavalent substitution, $CaMn_{1-x}Mo_xO_3$.[22] In both series, each W^{6+} or Mo^{6+} ion creates two electrons in the Mn sublattice, so that the electron-doping rate is faster with this substitution than in $CaMnO_3$ substituted on B-sites by pentavalent cations (like Nb, Ta, or V). There is neither A-site structural disorder nor A-site magnetic contribution associated with magnetically active lanthanide, but the W or Mo cations induce defects that affect the transfer of e_g electrons in the Mn sublattice. The ferromagnetic double-exchange interactions, linked with "shared" e_g electron between two neighboring Mn (via O), are largely reduced, which is manifested by lower electric conductivity compared to A-site-substituted $CaMnO_3$ at the same electron doping. Even if the metallic character is retained for $x = 0.04$, the maximum observed moment of 0.4 μ_B is about twice smaller than for $Ca_{0.92}Sm_{0.08}MnO_3$. It is worth mentioning that a similar effect is observed for the Nb^{5+}- or Ta^{5+}-substituted $CaMnO_3$.[18] In these pentavalent systems, an even more drastic reduction of the double exchange takes place, and in particular, the maximal bulk magnetization reaches only 0.2 μ_B for 6% of substitution. This suggests that the mobility of e_g electrons is more strongly influenced by the quantity of defects than by their formal valence. The concomitant decrease of e_g electron mobility and conservation of metallicity suggest that the charge defects are effectively screened by electrons at the e_g band bottom,[36] only the itinerant electrons at Fermi level become "heavier" and more scattered.

An interpretation of these data can be proposed by using the description of the temperature dependence of the thermoelectric power for electron-doped manganites introduced by some of us.[37] The model applies to e_g electrons on a cubic lattice, interacting via oxygen. For the sake of comparing different systems, we set the energy difference between the e_g and p levels to a common and generally accepted value, namely 2 eV. As a result, we are left with two free parameters: t^z_z which represents the effective Mn−O hopping amplitude, and E_0, which stands for the ratio L^{12}/L^{11}. Typical values for the resulting bandwidth W, which follow from t^z_z, are close to 0.5 eV ($W \approx 0.43$ eV for $CaMn_{0.86}Mo_{0.04}O_3$[37]), whereas $E_0 \approx -10$ meV ($E_0 \approx -16$ meV for $CaMn_{0.86}Mo_{0.04}O_3$). Let us stress that good agreement between the theoretical curve and experimental data is only achieved in a narrow range of parameters. The result of this analysis is presented in Figure 13. We start with $CaMn_{0.96}W_{0.04}O_3$, first assuming that the charge carrier density n is the nominal one, $n = 0.08$. In this case, a good agreement with the experimental data is obtained for $W = 0.40$ eV and $E_0 = -12$ meV. These values are compatible with the ones previously reported.[37] Nevertheless, using the same W value to analyze the $x = 0.02$ sample yields only a poor agreement, even though one expects that both samples

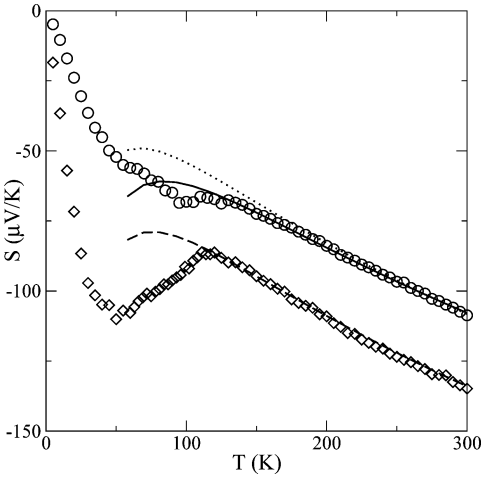

Figure 13. Thermopower of $CaMn_{0.96}W_{0.04}O_3$ (circles) and $CaMn_{0.98}W_{0.02}O_3$ (diamonds). Theoretical calculations for $n = 0.08$, $W = 0.4$ eV, $E_0 = -12$ meV (dotted line), $n = 0.106$, $W = 0.33$ eV, $E_0 = -14$ meV (full line); and for $n = 0.074$, $W = 0.33$ eV, $E_0 = -11$ meV (dashed line).

should be characterized by the same W. We therefore reanalyzed both samples by allowing the carrier density to slightly deviate from the nominal value. We indeed obtained a significantly better agreement to the $x = 0.04$ sample for $n = 0.106$ and $W = 0.33$ eV, and for $n = 0.074$ and $W = 0.33$ eV to the $x = 0.02$ sample. This question of the actual carrier density will be discussed later. Having obtained a consistent parameter set, we can compare it to the case of substituting with Mo. In that case, the same analysis yields $W = 0.43$ eV, which is larger than in the W-substituted sample. We therefore deduce that the W^{6+} ions more effectively scatter the e_g electrons than the Mo^{6+} ions. As a result, we expect that ordering temperatures will be higher for the W-substituted samples, which is indeed compatible with the resistivity and magnetic measurement presented above.

This model is valid in the case of small doping, when S varies linearly at high T ($x \leq 0.12$). For larger x ($x = 0.15$), the thermopower tends to a weakly temperature-dependent value above T_{OO}. This value is very similar to that observed in $Ca_{0.65}Sm_{0.35}MnO_3$ (measured, however, only up to 300 K, so the high-temperature behavior is not exactly known),[34] in which the Mn valency is equal to 3.65. Empirically, we find a good agreement between a simple configurational entropy term (Heikes formula) and charge-carrier concentration presumed from chemical formula, i.e., -53μV/K for $x = 0.15$.[38] In $Ca_{1-x}La_xMnO_3$ ($0.4 \leq x \leq 0.9$), i.e., for the A-site-substituted system, it has been, however, argued that S varies as $1/T$ at high temperatures and tends to a constant value close to $-19\ \mu$V/K, independently of x.[39] This constant was intuitively linked to spin entropy of Mn^{3+}/Mn^{4+} background. In $CaMn_{0.85}W_{0.15}O_3$, this behavior is not reproduced and the Seebeck coefficient can be simply explained considering only the doping term of the Heikes formula, such as if any additional entropy, including that of spin background, remains quenched up to high temperatures. We note that the explanation of the thermoelectric power is still a

(35) Pissas, M.; Margiolaki, I.; Prassides, K.; Suard, E. *Phys. Rev. B* **2005**, *72*, 064426.
(36) Ziman, J. M.; *Principles of the Theory of Solids*; Cambridge University Press: Cambridge, U.K., 1964; p 131.
(37) Frésard, R.; Hébert, S.; Maignan, A.; Pi, L.; Hejtmanek *Phys. Lett. A* **2002**, *303*, 223.
(38) Chaikin, P. M.; Beni, G. *Phys. Rev. B* **1976**, *13*, 647.
(39) Palstra, T. T. M.; Ramirez, A. P.; Cheong, S. W.; Zegarski, B. R.; Schiffer, P.; Zaanen, J. *Phys. Rev. B* **1997**, *56*, 5104.

matter of controversy; nonetheless, a possible discrepancy between proposed explanations for $Ca_{1-x}La_xMnO_3$ and $CaMn_{0.85}W_{0.15}O_3$ ($Ca_{0.65}Sm_{0.35}MnO_3$) can just lie in a more localized carrier because of higher distortion (due to Sm-for-Ca substitution) or strong perturbation of conducting MnO_6 network (due to W-for-Mn substitution).

An interesting finding in the region of C-type AFM phases of the $CaMn_{1-x}W_xO_3$ system is the exceptionally high orbital order temperature, reaching $T_{OO} \cong 370$ K for $x = 0.12$. Because the itinerancy of electrons is reduced in the present system, the stabilization of the ferrodistortive OO cannot originate from the e_g electron delocalization in the FM chains of the C-type phase. Instead, it should be related to the formation of static $Mn^{3+}O_6$ distortions and their interactions via homogeneous strain field, i.e., to the cooperative Jahn−Teller effect.

The reasons for exceptionally high critical temperature for charge order in the third compositional region are also not yet clear. The presence of W in the Mn sublattice disturbs a regular Mn^{3+}/Mn^{4+} ordering, but on the other hand, the electron delocalization is largely suppressed up to high temperatures, which may be favorable for high T_{CO}. The origin of particularly high structural transition temperatures is thus probably the same for both orbital and charge ordering. The ionic size of W^{6+} (0.60 Å), intermediate between 0.53 and 0.64 Å for Mn^{4+} and Mn^{3+} respectively, probably minimizes the local strain because of the size mismatch.[40] Moreover, the electronic configuration d^0 minimizes the magnetic disorder on the Mn sublattice and there are no magnetic interactions with the A-sublattice. A link could be done with the Mn^{4+}-rich Ruddlesden−Popper $n = 1$ phases, where high T_{CO} values are also observed because of the weaker interactions between the next-nearest Mn (in connection with the 2D character of the structure).[41,42]

Considering that the Mo^{6+} ions possess the same inactive d^0 electronic configuration and have a size (0.59 Å) similar to that of W^{6+}, it is not clear why the transition temperatures T_{OO} and T_{CO} are significantly higher in the W-based systems. As a tentative explanation, we speculate that the different electronegativity as well as the $\Delta G(T)$ Ellingham diagram dealing with W and Mo could be parameters to take into account. In fact, W and Mo do not behave in a similar way in such oxides, as shown by the existence of the double perovskite Ca_2MnWO_6,[30] whereas no information (to the best of our knowledge) is reported about Ca_2MnMoO_6. That could be probably connected with the easier stabilization of Mo^{+5} (than W^{+5}) as demonstrated in Ca_2FeMoO_6.[43] A Mo^{+5}/Mo^{+6} mixed valence could thus be less efficient at inducing localization than W^{+6}.

Another interesting aspect of the charge ordering is the same q value observed at low temperatures for a whole range of x in both the Mo- and W-based manganites. The cationic composition and the oxygen content were checked for the $x = 0.14$ sample, for which a 0.23 value of the modulation vector is observed. These characterizations do not refer to any shift in the Mn valence due to an oxygen or cationic nonstoichiometry, and the incommensurate ordered structure should be attributed to a pinning of the modulation vector at the particular value $\vec{q} \cong 0.23\vec{a}^*$. It is clear that further investigations are needed to understand the phenomena involved in these systems. In fact, a very small variation in the actual composition (in the limit of the error, whatever the characterization type) will induce small shifts in the Mn valence, which could explain the open questions previously mentioned about the q values or the TEP parameters. In these compounds, parameters such as oxygen content and Mn/W and Ca/(Mn + W) ratios can all vary simultaneously. Because of the stronger localization of the carrier in this system, in connection with the static repartition of the foreign elements on the Mn sublattice, the actual distribution of the cations may play a role in the observed properties. Moreover, short-range cationic ordering could also play a role, in agreement with the observation of double perovskites for $x \geq 0.2$. Another point in favor of a possible importance of the cationic distribution is the fact that as soon as the CO/OO appears (that is in small area of the $x \cong 0.12$ sample), the typical value $\vec{q} \cong 0.23\vec{a}^*$ is observed, which is close to the expected value $\vec{q} \cong 0.24\vec{a}^*$; the difference between observed and theoretical values then increases with x. It is likely that there is a kind of threshold (around 10%) upon the B-sublattice, as there is one at a similar value on the A-site framework, for which the nature of the interactions change.

To provide a better description of these compounds, it is necessary to know in detail and with a high accuracy the crystal structure (interatomic distances, tilting of the octahedra, etc.). Consequently, a neutron diffraction study versus temperature of $CaMn_{0.86}Mo_{0.14}O_3$ and $CaMn_{0.86}W_{0.14}O_3$ is under way.

Conclusion

A structural and magnetic phase diagram is proposed for the $CaMn_{1-x}W_xO_3$ system ($0 \leq x \leq 0.16$) that shows a similar succession of three phases with different ground states, as in the Mn^{4+}-rich side of the $Ca_{1-x}Ln_xMnO_3$ series. Three compositional regions of different ground states can be distinguished and, by comparison with the Mo series, associated with G-type AFM with a weak FM component, C-type AFM associated with orbital ordering, and Mn^{3+}/Mn^{4+} charge and orbital ordered AFM arrangement. This study demonstrates lower itinerancy of doped electrons in the high-temperature region, which is favorable for stabilization of OO in the C-type region and CO/OO for higher x values. Tungsten ions induce a large amount of Mn^{3+} in the matrix, but also a strong localization by impurity scattering, suppressing double exchange. Such a situation is favorable for orbital and/or charge ordering at high temperatures, around 380 K.

Acknowledgment. The authors acknowledge ECONET (10188YD-EGIDE) and SCOOTMO: HRPN-CT-2002-00293 for financial support.

CM0710958

(40) Rodriguez-Martinez, L. M.; Attfield, J. P. *Phys. Rev. B* **1996**, *54*, R15622.
(41) Sternlieb, B. J.; Hill, J. P.; Wildgruber, U. C.; Luke, G. M.; Nachumi, B.; Moritomo, Y.; Tokura, Y. *Pys Rev. Lett.* **1996**, *76*, 2169.
(42) Ibarra, M.; Retoux, R.; Hervieu, M.; Autret, C.; Maignan, A.; Martin, C.; Raveau, B. *J. Solid State Chem.* **2003**, *170*, 361.
(43) Alonso, J. A.; Casais, M .T.; Martinez-Lopez., M. J.; Martinez, J. L.; Velasco, P.; Munoz, A.; Fernandez-Diaz, M. T. *Chem. Mater.* **2000**, *12*, 161.